Single-molecule imaging of glycan-lectin interactions on cells with Glyco-PAINT

Riera, R.; Hogervorst, T.P.; Doelman, W.; Ni, Y.; Pujals, S.; Bolli, E.; ... ; Albertazzi, L.

nature chemical biology

ARTICLES

https://doi.org/10.1038/s41589-021-00896-2

Check for updates

Single-molecule imaging of glycan–lectin interactions on cells with Glyco-PAINT

Roger Riera[1,6], Tim P. Hogervorst[2,6], Ward Doelman[2], Yan Ni[3], Silvia Pujals[4], Evangelia Bolli[5], Jeroen D. C. Codée[2], Sander I. van Kasteren[2]✉ and Lorenzo Albertazzi[1,4]✉

Most lectins bind carbohydrate ligands with relatively low affinity, making the identification of optimal ligands challenging. Here we introduce a point accumulation in nanoscale topography (PAINT) super-resolution microscopy method to capture weak glycan–lectin interactions at the single-molecule level in living cells (Glyco-PAINT). Glyco-PAINT exploits weak and reversible sugar binding to directly achieve single-molecule detection and quantification in cells and is used to establish the relative k_{on} and k_{off} rates of a synthesized library of carbohydrate-based probes, as well as the diffusion coefficient of the receptor–sugar complex. Uptake of ligands correlates with their binding affinity and residence time to establish structure–function relations for various synthetic glycans. We reveal how sugar multivalency and presentation geometry can be optimized for binding and internalization. Overall, Glyco-PAINT represents a powerful approach to study weak glycan–lectin interactions on the surface of living cells, one that can be potentially extended to a variety of lectin–sugar interactions.

Lectins are sugar-binding proteins that play a pivotal role in many biological phenomena[1,2]. The interaction of carbohydrates with lectins enables the recognition of pathogens, which is crucial for the immune system, in particular in the case of innate immunity[3]. Lectins in the immune system have evolved to bind to carbohydrate pathogen-associated molecular patterns on the surface of bacteria and viruses. Immune cells recognize the geometry, number and sugar type of the carbohydrate arrangements on the pathogen membrane[4]. While the binding affinity involved in a single lectin–carbohydrate interaction is weak, the presence of multiple copies of the same carbohydrate in close proximity increases the strength of the interaction via multivalent effects[5,6]. These multivalent effects are influenced by carbohydrate configuration, glycan density and spatial arrangement, increasing the complexity involved in lectin-based carbohydrate recognition. The recognition of pathogens by lectins can induce different responses, such as pathogen uptake via endocytosis and immune cell activation, and hence the understanding of carbohydrate–lectin interactions will help improve the design of novel therapies such as the targeting of vaccines.

The mannose receptor (MR, or CD206) is a crucial lectin involved in shaping the immune response against pathogens. It is a multidomain endocytic receptor that is mainly present on the cell membrane of macrophages and a subset of dendritic cells[7]. The MR has eight C-type lectin domains (CTLDs) able to bind mannosides in a calcium-dependent manner and one cysteine-rich domain (CRD) that can bind sulfated carbohydrates in a calcium-independent manner[8,9]. The eight CTLDs share little homology and have different affinities for mannosides, which lie in the high-nM to μM range[10,11]. The receptor is able to dimerize, and both the monomeric and dimeric forms are able to bind, carbohydrates[12,13]. The MR plays a role as a pathogen-recognizing receptor able to induce maturation of immune cells following stimulation with mannosides. Additionally, the binding of pathogens can induce receptor-mediated endocytosis and trafficking of pathogens towards early endosomes[14,15]. Therefore, the MR has been targeted to improve antigen (cross-)presentation.

Despite the role of the MR in these processes, details of carbohydrate–MR interactions in relation to its function are not yet resolved[8,16], something that also holds for several other lectins[17]. The MR has multiple conformations, in which the domain orientation is severely altered[13,18] and the receptor itself is glycosylated (which can result in the interaction of the MR with other lectins and in *cis*-competition[7]), complicating the study of sugar-receptor-binding. The study of carbohydrate–MR interactions has therefore focused on the in vitro quantification of binding of specific sugars, under either static or flow conditions, to determine binding preferences (for example, surface plasmon resonance (SPR)[19], fluorescence-based assays[19,20] and enzyme-linked immunosorbent assay[21]). On cells and in vivo, the focus has generally been on studying the effect of removal of the MR by knockout[22–24] or blockage of its interaction with antibodies[25,26]. However, none of these approaches can recapitulate the complexity and subtlety of the carbohydrate–lectin interaction. A technique that could provide kinetic information on the surface of live cells would therefore be of great value in elucidating the precise role of carbohydrate–lectin binding in their biological functions.

Point accumulation in nanoscale topography is a fluorescent, single-molecule, super-resolution microscopy technique based on the exploitation of weak interactions[27,28] (Fig. 1a). PAINT, like other single-molecule, super-resolution techniques, is based on the detection, localization and counting of individual molecules and it requires that only a sparse subset of the target molecules are emitting at any one time. PAINT achieves this by coupling the fluorescent

[1]Department of Biomedical Engineering, Institute for Complex Molecular Systems, Eindhoven University of Technology, Eindhoven, the Netherlands. [2]Department of Bio-Organic Synthesis, Leiden Institute of Chemistry, Leiden University, Leiden, the Netherlands. [3]Laboratory of Chemical Biology, Department of Biomedical Engineering and Institute for Complex Molecular Systems, Eindhoven University of Technology, Eindhoven, the Netherlands. [4]Nanoscopy for Nanomedicine, Institute for Bioengineering of Catalonia, Barcelona, Spain. [5]Cellular and Molecular Immunology, Bioengineering Sciences Department, Vrije Universiteit Brussel, Brussels, Belgium. [6]These authors contributed equally: Roger Riera, Tim P. Hogervorst.
✉e-mail: s.i.van.kasteren@chem.leidenuniv.nl; l.albertazzi@tue.nl

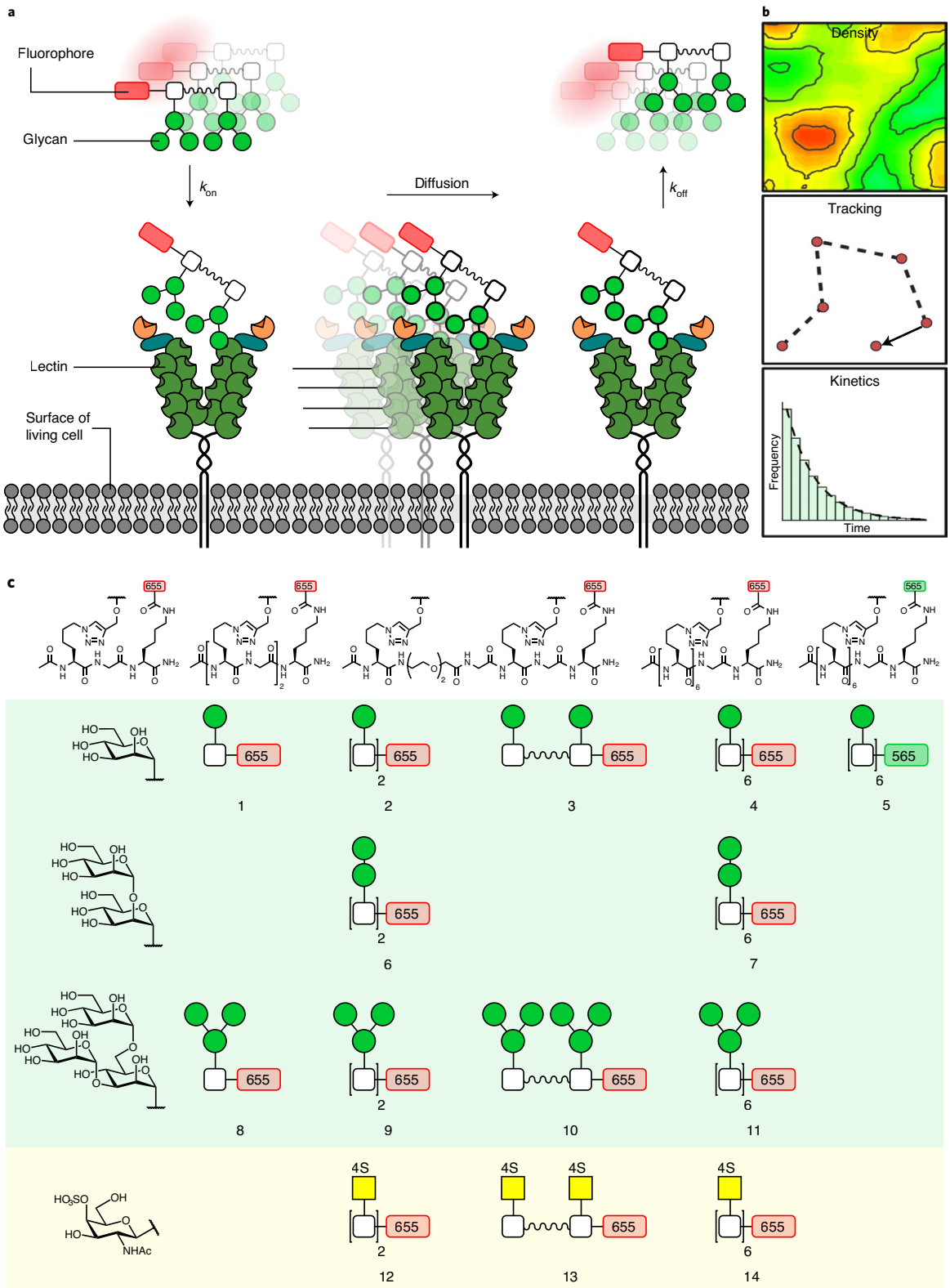

Fig. 1 | Scheme of the Glyco-PAINT procedure. a, A probe consisting of a fluorophore (depicted in red) linked to a glycan cluster (green) becomes visible when binding to the cell surface mannose receptor. **b**, Imaging the bound fluorescent ligand is used to determine the on-cell receptor density, tracking receptor movement, and quantify the binding kinetics of the glycans. **c**, The library of different mannose receptor ligands used, including ligands for the C-type lectin domains (dark green) and cysteine-rich domain (yellow) of the receptor.

emitter to a freely diffusing probe in solution that is detected by the camera only when it interacts with the molecule of interest, since the fluorescence of single emitters is not blurred by diffusional motion and it appears as defined puncta. Therefore, it requires transient interactions in the millisecond–second range so that the labeled probe is bound for a sufficient length of time for

detection but detaches shortly after so that there is no spatial overlap with newly incoming probes. Given the dissociation constant, K_D, of the specific interaction, the bound fraction of receptors can be tuned by changing the concentration of probes in solution so as not to saturate the image of fluorescent puncta. Accumulation of these binding events over time allows reconstruction of a complete map of receptors on the cell surface. To date, these transient interactions are mostly achieved by DNA–DNA hybridization (DNA–PAINT), while the use of other molecular interactions has been explored[29,30], for example, in universal PAINT[31,32]. We realized that weak native glycan–lectin interactions would be well suited for use in a PAINT-based approach to study the interaction of the MR with different multivalent carbohydrate ligands on the surface of living cells.

Here we report on a Glyco-PAINT-approach to the imaging and localization of ligands bound to MRs on the surface of live cells at nanometric spatial resolution. This approach allows study of the kinetic parameters of MR–glycan interactions and diffusion of the membrane-bound receptor. We synthesized a library of mannoside probes and studied the trends of k_{on} and k_{off} depending on mannose valency and structure. We hypostatize that rebinding has an important role in multivalent glycan interactions with the MR. By tracking diffusion of the receptor–glycan complex on the cell surface, we found no effect of the different multivalent ligands on the oligomeric state of the receptor. Finally, we could correlate the relative binding affinity and binding strength to the rate of ligand internalization, an important parameter for applications such as antigen presentation. Our method allows the establishment of quantitative kinetic parameters of the weak carbohydrate–lectin interactions of complex carbohydrates in living cells and paves the way for the study of various lectin–carbohydrate interactions.

Results

Glyco-PAINT approach and glycan probes. Here we show how mannose–MR interactions can be successfully used to perform PAINT microscopy, as schematically represented in Fig. 1a. The labeled glycan probes in solution can bind to the MR on live cells and diffuse together with the receptor until unbinding. Due to weak glycan–lectin affinity, this interaction shows kinetics in the range where PAINT usually operates. Imaging of binding–unbinding events results in three quantitative readouts at the single-molecule level (Fig. 1b): (1) density and spatial distribution of binding events; (2) diffusion of the receptor–sugar complex; and (3) residence time of the carbohydrate on the MR. These can be used to establish the relative binding kinetics (k_{on} and k_{off}) and explore the effect of glycans on receptor dynamics. To explore variations in ligand binding to the MR, we synthesized a library of fluorescently labeled carbohydrate clusters while varying the number and nature of the carbohydrate (Fig. 1c)[33]. Ligands for both the CTLD (mono-, α1,2-di and α1,3-α1,6-trimannoside) and the CRD (sulfo-GalNAc) were introduced on a fluorescent peptide carrier scaffold in different stoichiometries (one, two or six glycans per peptide), or with different spacings (one or four amino acid spacers between the constructs modified with two glycans). A nonfluorescent variant of the CTLD-binding glycans was also synthesized to obtain a 'dark cluster' (**23**) (Supplementary Fig. 7). This library allows study of structure-activity relations in lectin binding, varying multivalency and geometry of presentation.

Live-cell sugar–lectin binding rate measurements. We studied MR–glycan interactions using a CHO-K1 cell line stably expressing the murine MR gene (*Mrc1*). This cell line expresses the unmodified version of the MR at a stable level across all cells, independent of its activation states (which can lead to variation in MR expression levels in primary immune cells). Other lectins that can potentially bind fluorescent ligands, such as DC-SIGN and Langerin and which are present on immune cells, are absent on this cell line and therefore do not complicate the interpretation of binding events. Moreover this cell line offers an ideal negative control (nonexpressing cells), supporting the validation of the method.

As a first test of the approach, probe **4** was added to the cell medium (5 nM) and visualized in real time using a total internal reflection (TIRF) microscope. Binding of individual probes to the MR on the cell membrane was observed as bright fluorescent puncta (Fig. 2a), with each bright spot corresponding to a single binding event. Fitting of a Gaussian function to these bright spots allows determination of the position of the receptor at nanometeric precision[34]. We obtained an average localization precision of 19 nm, in accordance with previous work on PAINT in live cells[31,35]. Acquisition of fluorescence over a 15-min period allowed sufficient datapoint collection to determine the distribution of the MR on the membrane, as shown in Fig. 2b. Continuous diffusion of the MR through the cellular membrane in living cells means that the images obtained represent a density map of the distribution of receptors on the surface, rather than a static picture. In this setting, uniform distribution of the MR on the CHO-MR was observed, rather than the localized accumulation of lectins observed on dendritic cells[36].

The reconstructed density maps also yielded information about binding kinetics. The second-order rate of the binding reaction (r) depends on the rate constant k_{on}, the density of receptors on the cell $[R]$ and the concentration of the probe $[L]$ (equation (1)). By having a fixed probe concentration $[L]$ and assuming equal receptor density $[R]$ across experiments, the relative k_{on} of the different ligands for the receptor was determined by measuring the density of binding events on the cell membrane. Figure 2c shows the reconstructed maps for all probes synthesized (brightfield images are shown in Supplementary Fig. 1), while in Fig. 2d the quantification of the density of binding events, a relative measure of k_{on}, is presented.

$$r = k_{on} * [R] * [L] \quad (1)$$

The mannoside probe library allowed us to study the effect on k_{on} of both mannoside configuration (mono-, di- or trimannoside or sulfo-GalNAc) and the number of carbohydrate copies per probe. We first compared constructs with the same type of mannose cluster geometry but different number of copies (one, two or six). We observed that the number of copies has a strong effect on k_{on}, because hexavalent probes (**4**, **7** and **11**) clearly display relative k_{on} rates five- to tenfold higher than monovalent analogs. This shows the ability of multivalent binding to increase lectin affinity over an order of magnitude. Similar trends were observed for K_D values determined by SPR (Supplementary Fig. 2 and Supplementary Table 1).

Comparing compounds with the same valency but different mannose configurations (mono-, di- and tri-mannose), it appears that configuration plays a less important role in determining k_{on}. For example, the three probes with six mannosides (**4**, **7** and **11**) elicited no significant difference despite the different total number of mannose sugars ($P > 0.05$). This suggests that, with our design, we are approaching a maximum k_{on} since mannose configuration actually plays a major role in bivalent probes (**2**, **6** and **9**) with lower affinity. This is also supported by the fact that there is no significant difference within the bivalent trimannoside (**9**) probe and the remainder of the hexavalent probes (**4**, **7** and **11**), meaning probe **9** has also reached this plateau and increasing the valency of this configuration does not increase affinity further ($P > 0.05$).

Sulfated sugars deserve a separate discussion. The binding on-rate of the bivalent sulfo-GalNAc probe (**12**) and the hexavalent sulfo-GalNAc probe (**14**) are similar and fivefold lower than CTLD-binding probes (**2** and **4**, respectively). This could be due to the single CRD per MR (compared to eight of the CTLDs) or an intrinsic lower affinity of this domain for its known ligands[37].

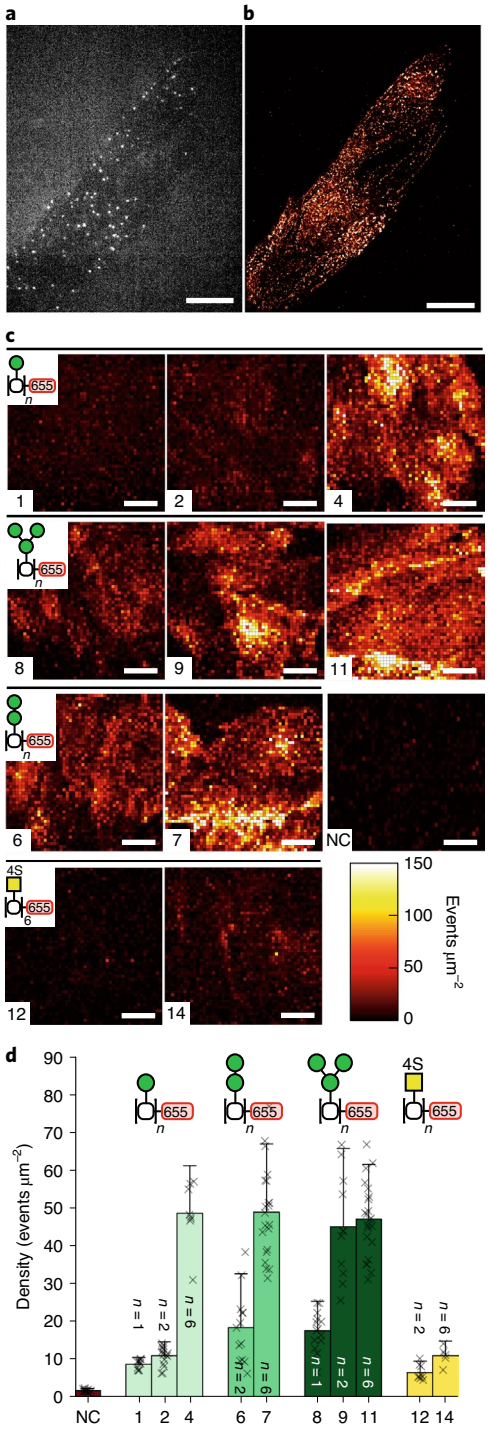

Fig. 2 | Live cell imaging of the MR with the Glyco-PAINT approach. **a**, Diffraction-limited image of single-ligand–receptor binding. **b**, Reconstructed image of a MR on a group of cells derived from the accumulation of multiple binding events over time. **c**, Density map of trajectories detected by SPT (density measured in trajectories µm^{-2}). Negative control was obtained by imaging probe **4** on CHO cells not expressing the MR. **d**, Quantification of the density of trajectories in ten cells (mean ± s.d.). Negative control of probe **4** on non-MR-expressing CHO cells (NC, dark red), monomannosides (**1**, **2** and **4**, light green), α1,2-dimannosides (**6** and **7**, green), α1,3-α1,6-trimannosides (**8**, **9** and **11**, dark green) and sulfo-GalNAc (**14**, yellow). Scale bars, 10 µm.

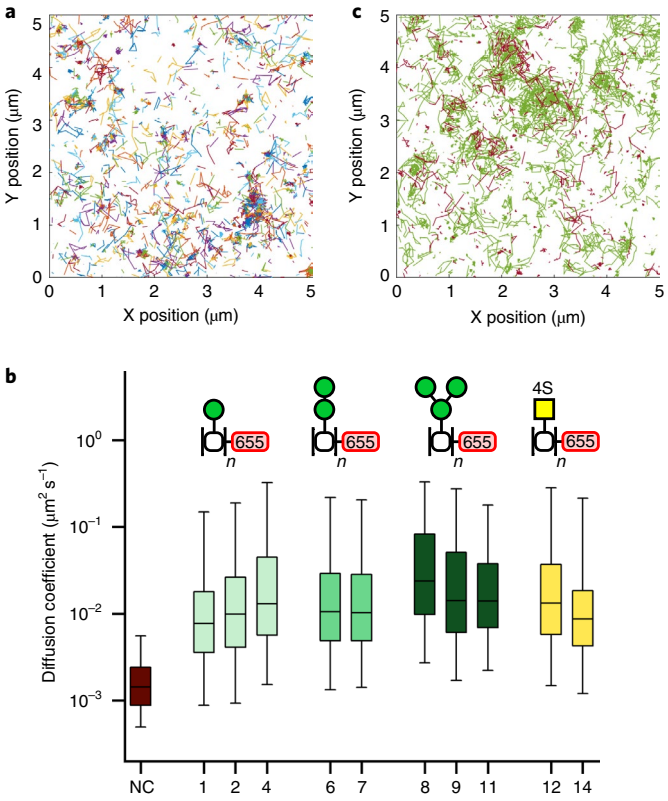

Fig. 3 | Lateral diffusion of the MR on the cell membrane. a, An example of a set of trajectories obtained with the hexavalent monomannoside probe (**4**). **b**, Distribution of the diffusion coefficient of our probe library calculated from trajectory mean square displacement. Box center represents median, box limits show 25th–75th percentiles and whiskers denote 5th–95th percentiles ($n = 50{,}000$ trajectories analyzed over 20 cells). Monomannosides (**1**, **2** and **4**, light green), α1,2-dimannosides (**6** and **7**, green), α1,3-α1,6-trimannosides (**8**, **9** and **11**, dark green), sulfo-GalNAc (**14**, yellow) and negative control (NC, calculated from localization precision). **c**, An example of trajectories obtained simultaneously: hexavalent monomannoside ATTO565 (**5**) in green and hexavalent sulfo-GalNAc ATTO655 (**14**) in red.

Overall, these measurements showed a clear structure-binding relationship of carbohydrates to the MR where the valency and domain type (CRD versus CTLD) dominate.

Multivalent mannoside probes do not promote MR clustering. During the above experiments, we observed movement of the fluorescent probe on the membrane. This is due to receptor two-dimensional diffusion during binding of the probe. In every frame, the position of the probe–receptor complex is localized with nanometric precision and, by linking these positions, it is possible to obtain their trajectory. We can calculate a variety of parameters such as velocity, type of diffusion and diffusion coefficient (in µm^2 s^{-1}) for each individual receptor and the average value over tens of thousands of trajectories. Notably, to avoid crossing of the trajectories of two fluorescent molecules during image acquisition, we reduced probe concentration to 1 nM and imaged 20 cells chosen randomly across the whole sample to acquire >50,000 trajectories per probe.

A representative example of the observed trajectories of the MR binding to probe **4** is shown in Fig. 3a. The different trajectories allowed us to calculate a diffusion coefficient for the receptor following binding to different ligands (Fig. 3b). The normalized distribution of diffusion coefficients indicates that all distributions are

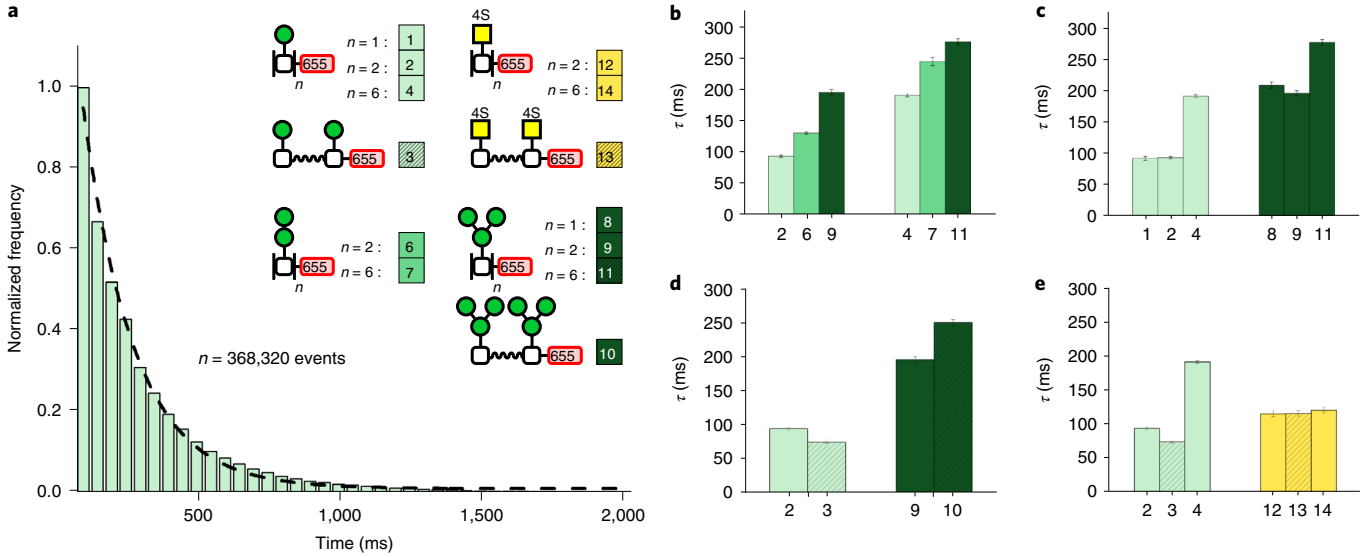

Fig. 4 | Dwell times and k_{off} of mannoside probes binding to the MR. a, An example of dwell time distribution and exponential decay fitting of hundreds of thousands of trajectories from the hexavalent monomannoside probe (**4**) binding on CHO-MR cells. **b–e**, Fitted τ values (fit value ± s.e.m., $n = 50{,}000$ trajectories over 20 cells) of monomannosides (**1**–**4**, light green), α1,2-dimannosides (**6** and **7**, green), α1,3-α1,6-trimannosides (**8**–**11**, dark green), sulfo-GalNAc (**12**–**14**, yellow) and spaced proves (diagonal stripes). **b,** Comparison between bivalent and hexavalent mannosides. **c,** Mono and trimannosides, **d,** Regular and spaced probes, **e,** Mannosides and sulfo-GalNAc probes.

similar and average around 0.01 μm s^{-1}. This is an important observation in analysis of the nature of sugar–lectin binding. The interaction of a multivalent sugar (one to six mannosides) with a multivalent receptor (eight CTLDs) could result in receptor clustering. However, the probes were probably too small to bridge multiple receptors during the residence time. To determine whether such a bridging event could take place, we attempted cross-linking of the receptors with mannan. However, this did not lower lateral diffusion of the receptor[38–42], as happens with mild fixation that cross-links the MR to adjacent molecules (Supplementary Fig. 3). Single-particle tracking is also a powerful tool to elucidate interactions by making use of the multicolor ability of fluorescence microscopy. Labeling two receptors with two spectrally separated colors allows temporal visualization of the relative positions of the two biomolecules, and obtaining information about their interactions (for example, codiffusion of a labeled complex) or partitioning in the membrane. To show the potential of Glyco-PAINT in performing multicolor single-particle tracking (SPT) we synthesized probes with a different dye and simultaneously tracked them. Figure 3c shows the trajectory of two different probes (**5** in green and **14** in red), demonstrating the suitability of Glyco-PAINT in multicolor tracking. Notably, a larger number of green tracks were detected due to the larger k_{on} of the green probe. No differences in diffusion coefficient or affinity were observed, suggesting that binding to the two domains of the lectin was independent.

Effect of multivalency on binding time and k_{off}. We next set out to establish the receptor dwell time (τ, the inverse of the kinetic dissociation rate constant k_{off}), which is known to affect downstream biological processes such as signaling and/or internalization of the complex[43]. Notably, it has been particularly troublesome to determine this parameter for the MR to date, due to the weak and reversible nature of mannose–MR binding[4,5,44]. We determined τ for individual mannoside–MR complexes by quantifying the length of time the fluorescent probes remained associated with the receptor (using the same SPT data as for measuring the diffusion coefficient). Over 50,000 events were then used to obtain the mean value of τ by fitting an exponential decay. As shown in Fig. 4a, the decay is well fitted with a single exponential, indicating that a single population of residence times (that is, all receptor–sugar complexes) have the same behavior. Several structural considerations can be obtained from the comparison of different probes in Fig. 4b–e (k_{off} values are shown in Supplementary Fig. 4).

First, average residence time varies among the different ligand configurations (Fig. 4b), with trimannosides (dark green) binding more strongly than di- and monomannosides (medium and light green, respectively). It is worth noting that the complexity of mannosides influences sugar dissociation (k_{off}) but not association (k_{on}; Fig. 2). This may be due to the higher tendency of rebinding of trimannosides, as can be seen by the complex SPR response of trimannosides compared to monomannosides (Supplementary Fig. 2b). As expected, residence time varies with the global valency of the probe, as shown in Fig. 4c, and this happens in a nonlinear fashion with the $n = 1$ and $n = 2$ constructs being very similar (for both mono- and trimannosides), with $n = 6$ residing substantially longer. The nonlinearity of binding rates is a key feature of multivalency[5,6]. Another important parameter for multivalency is the spacing between individual binders. To investigate this, we synthesized alternative bivalent probes equipped with a longer spacer between both mannosides using a triethylene glycol spacer matching the length of $n = 6$ probes. As a result, elongated probe **10**, featuring two trimannosides, bound better than the original bivalent probe **9** (Fig. 4d) and was almost equal to the hexavalent trimannoside probe **11**. The origin of this multivalent effect is probably rapid dissociation–rebinding, because the distance between two CTLDs on the same receptor is greater than that between carbohydrate moieties on a single cluster[45]. However, we did not observe the same behavior for monomannoside probes **2** and **3**, suggesting that the binding of mono- and trimannosides to the MR is qualitatively different. Lastly, Fig. 4e shows the residence times for different sulfated probes. Clearly residence time for all ligands is very similar, indicating that multivalent effects do not play an important role in this type of ligand. This is in agreement with the structural hypothesis that the CRD is monovalent.

Overall, these measurements show that k_{off} is sensitive to small changes in the valency and geometry of presentation in contrast

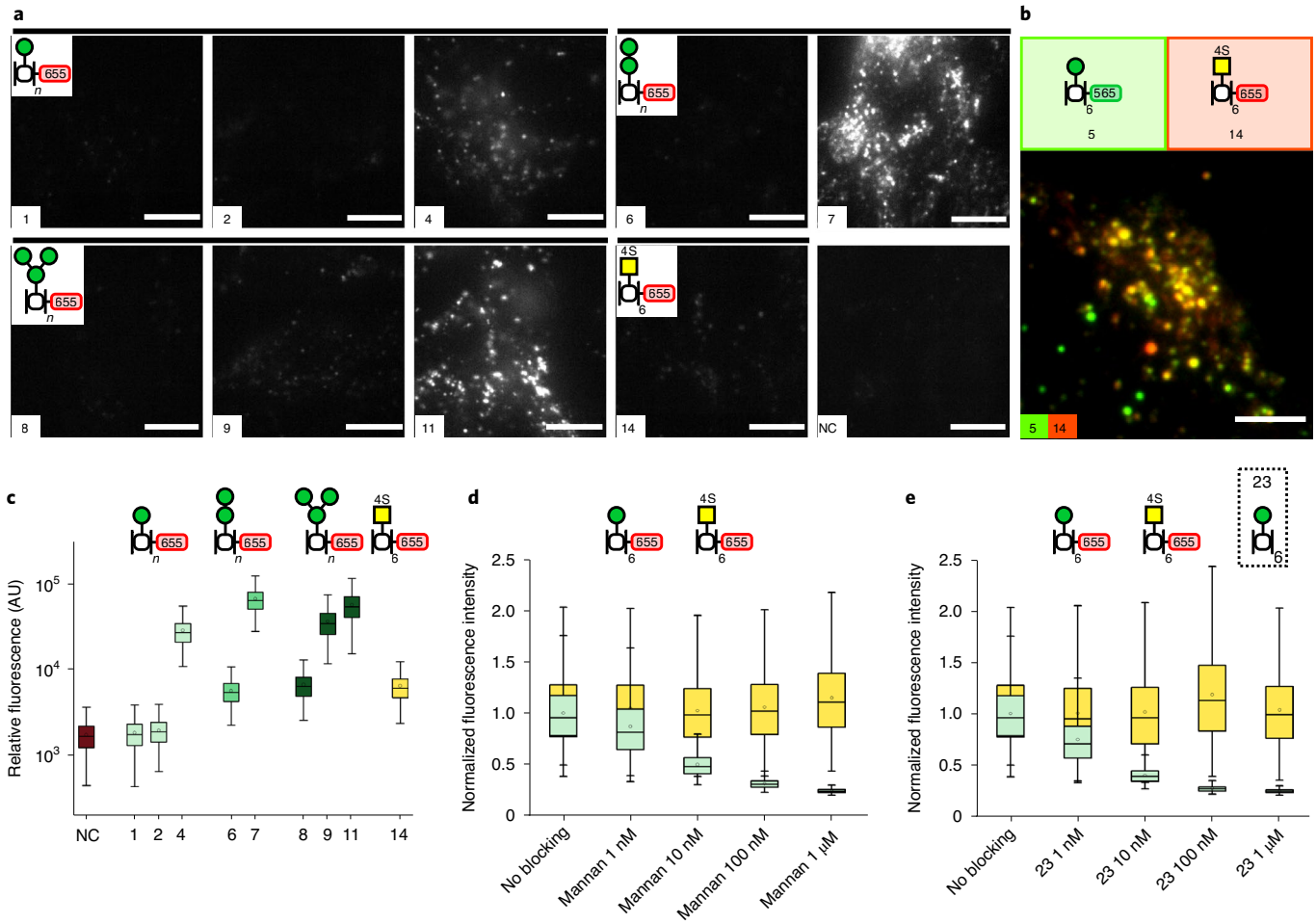

Fig. 5 | Cellular uptake of probes binding to the MR. a, Images of the cytoplasm of cells loaded with probes, using HILO illumination. **b**, Simultaneous internalization of ATTO565-labeled hexavalent monomannoside (**5**) and ATTO655-labeled hexavalent sulfo-GalNAc (**14**). **c**, Internalization as measured by flow cytometry. Negative control (NC, dark red), monomannosides (**1**, **2** and **4**, light green), α1,2-dimannosides (**6** and **7**, green), α1,3-α1,6-trimannosides (**8**, **9** and **11**, dark green) and sulfo-GalNAc (**14**, yellow). **d**, Blocking the binding of hexavalent monomannoside (**4**) and hexavalent sulfo-GalNAc (**15**) with different concentrations of nonlabeled mannan. **e**, As in **d**, but using the nonlabeled hexavalent monomannoside (**23**) rather than mannan. Scale bars, 10 µm (**a**), 1 µm (**b**). Box plot centers represent median, box limits 25th–75th percentiles, whiskers 5th–95th percentiles and mean is represented as a circle. All flow cytometry measurements had $n = 10.000$ cells. AU, arbitrary units.

to milder effects for k_{on} and the diffusion coefficient. These results indicate that k_{off} is the most suitable parameter for tuning the control of sugar–MR interactions.

Affinity-dependent cellular uptake. Because the MR cycles between the surface and an endolysosomal pool[46–48], it has been used to target vaccines and drugs to these cellular compartments in antigen-presenting cells[7,49]. However, a correlation between specific ligand affinities and cellular uptake has never been quantified for the MR. We therefore attempted to establish whether any of the above-measured parameters correlated to internalization of MR-bound ligands. We tested the internalization of mannosides by incubating cells with different constructs at 20 nM concentration for 2 h and detection of intracellular fluorescence by either microscopy or flow cytometry. Figure 5a shows the highly inclined illumination (HILO)[50] images of all the synthesized probes. In this case, HILO illumination was used rather than the TIRF illumination previously used in the Glyco-PAINT images, as the former reaches further into the sample and allows imaging of the cytoplasm. We observed that fluorescence intensity was punctate, indicating endolysosomal uptake. We also observed a wide range in uptake magnitude of the different ligands (Fig. 5a). The hexavalent probes (**4**, **7**, **11** and **14**) were all taken up efficiently compared with the others. The uptake of these glycans was shown to be specifically driven by the MR because the CHO-K1 cells not expressing the receptor did not internalize the probes (see negative control on the bottom right in Fig. 5a), but appears independent of the lectin domain that is engaged because both CRD and CTLD ligands demonstrated uptake.

These qualitative trends in internalization levels were further quantified using flow cytometry (Fig. 5c). Again, the four hexavalent probes (**4**, **7**, **11** and **14**) displayed the highest internalization levels, more than one order of magnitude higher compared with the mono- and bivalent probes. This suggests that multivalency is an important parameter for uptake. However, the α1,3-α1,6-trimannoside configuration also seemed to perform better than the other two configurations, similar to what we observed in binding parameters.

We also decided to study the interaction between the CTLD and CRD ligation, to determine whether prebinding of one domain would affect the affinity and behavior of the other. Cells were therefore incubated with ATTO565-labeled (green) hexavalent monomannoside (**5**) together with the ATTO655-labeled (red) hexavalent sulfo-GalNAc probe (**14**). Internalization of both

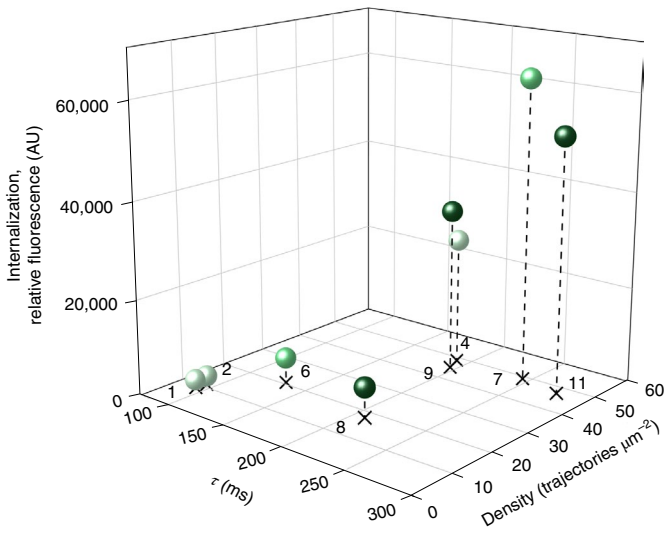

Fig. 6 | Correlation of kinetic parameters with cellular uptake. Correlation of residence time (inverse of k_{off}) and density of binding events on the cell surface (relative k_{on}) to the level of internalization as measured by flow cytometry.

probes was imaged (Fig. 5b), revealing that both are internalized with similar kinetics. Both probes were seen to accumulate in the same vesicle (yellow vesicles), as well as in distinct vesicles (Pearson coefficient = 0.73), suggesting no interplay between the domains in terms of uptake. This was further confirmed by a series of flow-cytometry-based blocking assays. Either the hexavalent monomannoside (**5**) or the hexavalent sulfo-GalNAc probe (**14**) was incubated in the presence or absence of 1 nM to 1 mM of either the CTLD ligand mannan (Fig. 5d), or the unlabeled variant of the hexavalent monomannoside **23** (Fig. 5e). Both reagents blocked the uptake of mannose-based clusters in a concentration-dependent manner but did not impinge on sulfo-GalNAc uptake. This suggests that binding to different domains is independent and nonexclusive (that is, the same receptor can interact simultaneously with either domain). If ligation of a carbohydrate to one of the domains was the specific trigger for internalization, alteration in internalization of the other ligand should have been observed; this was not observed, supporting the hypothesis that internalization is not triggered by binding but is rather the result of receptor recycling.

Structure–binding–activity relations. Glyco-PAINT revealed several characteristic binding parameters of mannosides at the single-molecule level. Combining these data with the functional internalization assay presented in the previous paragraph offers the opportunity to draw a quantitative picture of the structure–activity relations of individual mannosides. Figure 6 correlates, in a three-dimensional graph, where the two key parameters—relative k_{on} (shown as density) and k_{off} (shown as dwell time)—are related to functionality (cell uptake). It is apparent that there is a sharp transition between probes showing low functionality (bottom left, low k_{on} and high k_{off}) and those with strong internalization (top right, high k_{on} and low k_{off}). Moreover, it is clear that both high k_{on} and high residence are needed to trigger internalization. These measurements show the ability of Glyco-PAINT to reveal key properties in the exploration of sugar–lectin structure–activity relations.

Discussion

The intrinsically weak carbohydrate–lectin interactions render them perfectly suited for direct probing by a PAINT approach, as introduced here. The Glyco-PAINT methodology described was used to investigate the effect of glycan valency and geometry on binding and trafficking of the MR in living cells. The technique was used to determine kinetic binding parameters and the diffusion coefficient on cell membranes of multiple ligand configurations. This method allows quantitative determination of absolute k_{off} of the interactions while only relative k_{on} can be measured. The combination with other methods capable of accurate measurement of receptor density will allow the calculation of absolute k_{on} and a more complete picture of interaction kinetics.

It was revealed that the binding constant k_{on} reached a maximum value with the largest constructs tested, containing six mannosides in the clusters. The residence time on the receptor on the other hand increased linearly with the number of mannosides without reaching a plateau in the range studied. We also observed that binding of mannose clusters to the CTLDs of the MR proved to be notably stronger than that of sulfo-GalNAc to the cysteine-rich domain.

Mannose-binding lectins have found widespread application in targeted intracellular delivery of cargo, to enhance the uptake of therapeutic proteins and vaccines. Unlike the common in vitro methodologies used for the screening of ligands, Glyco-PAINT allowed us to directly correlate cell uptake of clusters to the different binding parameters in living cells. The results suggest that sufficient binding and residence time of the multivalent clusters on the receptor are required for effective uptake. Not only could this approach assist in the design and validation of new therapeutic targets for the MR, it could also be extended in the study of other relevant lectin–carbohydrate interactions on live cells such as DC-SIGN and Siglecs. Glyco-PAINT could help in elucidating the precise role of lectin–carbohydrate interactions in their biological functions, and in paving the way for the use of glycan clusters in a well-informed manner for their utilization in intracellular targeting of therapeutics and vaccines.

Online content

Any methods, additional references, Nature Research reporting summaries, source data, extended data, supplementary information, acknowledgements, peer review information; details of author contributions and competing interests; and statements of data and code availability are available at https://doi.org/10.1038/s41589-021-00896-2.

Received: 11 October 2020; Accepted: 10 September 2021;
Published online: 11 November 2021

References

1. Ghazarian, H., Idoni, B. & Oppenheimer, S. B. A glycobiology review: carbohydrates, lectins and implications in cancer therapeutics. *Acta Histochem.* **113**, 236–247 (2011).
2. Kumar, K. K. et al. Biological role of lectins: a review. *J. Orofac. Sci.* **4**, 20–25 (2012).
3. Holmskov, U., Thiel, S. & Jensenius, J. C. Collectins and ficolins: humoral lectins of the innate immune defense. *Annu. Rev. Immunol.* **21**, 547–578 (2003).
4. Dam, T. K. & Brewer, C. F. Lectins as pattern recognition molecules: the effects of epitope density in innate immunity. *Glycobiology* **20**, 270–279 (2010).
5. Lundquist, J. J. & Toone, E. J. The cluster glycoside effect. *Chem. Rev.* **102**, 555–578 (2002).
6. Kiessling, L. L., Gestwicki, J. E. & Strong, L. E. Synthetic multivalent ligands in the exploration of cell-surface interactions. *Curr. Opin. Chem. Biol.* **4**, 696–703 (2000).
7. Martinez-Pomares, L. The mannose receptor. *J. Leukoc. Biol.* **92**, 1177–1186 (2012).
8. Leteux, C. et al. The cysteine-rich domain of the macrophage mannose receptor is a multispecific lectin that recognizes chondroitin sulfates A and B and sulfated oligosaccharides of blood group Lewis A and Lewis X types in addition to the sulfated N-glycans of lutropin. *J. Exp. Med.* **191**, 1117–1126 (2000).
9. Fiete, D. J., Beranek, M. C. & Baenziger, J. U. A cysteine-rich domain of the 'mannose' receptor mediates GalNAc-4-SO_4 binding. *Proc. Natl Acad. Sci. USA* **95**, 2089–2093 (1998).

10. Biessen, E. L. et al. Lysine-based cluster mannosides that inhibit ligand binding to the human mannose receptor at nanomolar concentration. *J. Biol. Chem.* **271**, 28024–28030 (1996).
11. Blum, J. S., Stahl, P. D., Diaz, R. & Fiani, M. L. Purification and characterization of the d-mannose receptor from J774 mouse macrophage cells. *Carbohydr. Res.* **213**, 145–153 (1991).
12. Taylor, M. E. & Drickamer, K. Structural requirements for high affinity binding of complex ligands by the macrophage mannose receptor. *J. Biol. Chem.* **268**, 399–404 (1993).
13. Napper, C. E., Dyson, M. H. & Taylor, M. E. An extended conformation of the macrophage mannose receptor. *J. Biol. Chem.* **276**, 14759–14766 (2001).
14. Burgdorf, S., Kautz, A., Bohnert, V., Knolle, P. A. & Kurts, C. Distinct pathways of antigen uptake and intracellular routing in CD4 and CD8 T cell activation. *Science* **316**, 612–616 (2007).
15. Burgdorf, S., Schölz, C., Kautz, A., Tampé, R. & Kurts, C. Spatial and mechanistic separation of cross-presentation and endogenous antigen presentation. *Nat. Immunol.* **9**, 558–566 (2008).
16. East, L. & Isacke, C. M. The mannose receptor family. *Biochim. Biophys. Acta* **1572**, 364–386 (2002).
17. Garcia-Vallejo, J. J. & van Kooyk, Y. The physiological role of DC-SIGN: a tale of mice and men. *Trends Immunol.* **34**, 482–486 (2013).
18. Hu, Z. et al. Structural insights into the pH-dependent conformational change and collagen recognition of the human mannose receptor. *Structure* **26**, 60–71 (2018).
19. Frison, N. et al. Oligolysine-based oligosaccharide clusters: selective recognition and endocytosis by the mannose receptor and dendritic cell-specific intercellular adhesion molecule 3 (icam-3)-grabbing nonintegrin. *J. Biol. Chem.* **278**, 23922–23929 (2003).
20. Feinberg, H. et al. Structural analysis of carbohydrate binding by the macrophage mannose receptor CD206. *J. Biol. Chem.* **296**, 100368 (2021).
21. Kéry, V., Křepinský, J. J. F., Warren, C. D., Capek, P. & Stahl, P. D. Ligand recognition by purified human mannose receptor. *Arch. Biochem. Biophys.* **298**, 49–55 (1992).
22. Lee, S. J. et al. Mannose receptor-mediated regulation of serum glycoprotein homeostasis. *Science* **295**, 1898–1901 (2002).
23. DeSchoolmeester, M. L., Martinez-Pomares, L., Gordon, S. & Else, K. J. The mannose receptor binds *Trichuris muris* excretory/secretory proteins but is not essential for protective immunity. *Immunology* **126**, 246–255 (2009).
24. Dan, J. M., Kelly, R. M., Lee, C. K. & Levitz, S. M. Role of the mannose receptor in a murine model of *Cryptococcus neoformans* infection. *Infect. Immun.* **76**, 2362–2367 (2008).
25. Dangaj, D. et al. Mannose receptor (MR) engagement by mesothelin GPI anchor polarizes tumor-associated macrophages and is blocked by anti-MR human recombinant antibody. *PLoS ONE* **6**, e28386 (2011).
26. Martinez-Pomares, L. et al. Analysis of mannose receptor regulation by IL-4, IL-10, and proteolytic processing using novel monoclonal antibodies. *J. Leukoc. Biol.* **73**, 604–613 (2003).
27. Sharonov, A. & Hochstrasser, R. M. Wide-field subdiffraction imaging by accumulated binding of diffusing probes. *Proc. Natl Acad. Sci. USA* **103**, 18911–18916 (2006).
28. Jungmann, R. et al. Multiplexed 3D cellular super-resolution imaging with DNA-PAINT and Exchange-PAINT. *Nat. Methods* **11**, 313–318 (2014).
29. Delcanale, P. et al. Aptamers with tunable affinity enable single-molecule tracking and localization of membrane receptors on living cancer cells. *Angew. Chem. Int. Ed. Engl.* **59**, 18546–18555 (2020).
30. Kiuchi, T., Higuchi, M., Takamura, A., Maruoka, M. & Watanabe, N. Multitarget super-resolution microscopy with high-density labeling by exchangeable probes. *Nat. Methods* **12**, 743–746 (2015).
31. Giannone, G. et al. Dynamic superresolution imaging of endogenous proteins on living cells at ultra-high density. *Biophys. J.* **99**, 1303–1310 (2010).
32. Winckler, P. et al. Identification and super-resolution imaging of ligand-activated receptor dimers in live cells. *Sci. Rep.* **3**, 2387 (2013).
33. Li, R.-J. E. et al. Systematic dual targeting of dendritic cell C-type lectin receptor DC-SIGN and TLR7 using a trifunctional mannosylated antigen. *Front. Chem.* **7**, 650 (2019).
34. Small, A. & Stahlheber, S. Fluorophore localization algorithms for super-resolution microscopy. *Nat. Methods* **11**, 267–279 (2014).
35. Brockman, J. M. et al. Live-cell super-resolved PAINT imaging of piconewton cellular traction forces. *Nat. Methods* **17**, 1018–1024 (2020).
36. Neumann, A. K., Thompson, N. L. & Jacobson, K. Distribution and lateral mobility of DC-SIGN on immature dendritic cells–implications for pathogen uptake. *J. Cell Sci.* **121**, 634–643 (2008).
37. Liu, Y., Misulovin, Z. & Bjorkman, P. J. The molecular mechanism of sulfated carbohydrate recognition by the cysteine-rich domain of mannose receptor. *J. Mol. Biol.* **305**, 481–490 (2001).
38. Clayton, A. H. A. Fluorescence-based approaches for monitoring membrane receptor oligomerization. *J Biosci.* **43**, 463–469 (2018).
39. Gambin, Y. et al. Lateral mobility of proteins in liquid membranes revisited. *Proc. Natl Acad. Sci. USA* **103**, 2098–2102 (2006).
40. Naji, A., Levine, A. J. & Pincus, P. A. Corrections to the Saffman–Delbrück mobility for membrane bound proteins. *Biophys. J.* **93**, L49–L51 (2007).
41. Chung, I. et al. Spatial control of EGF receptor activation by reversible dimerization on living cells. *Nature* **464**, 783–787 (2010).
42. Low-Nam, S. T. et al. ErbB1 dimerization is promoted by domain co-confinement and stabilized by ligand binding. *Nat. Struct. Mol. Biol.* **18**, 1244–1249 (2011).
43. Corzo, J. Time, the forgotten dimension of ligand binding teaching. *Biochem. Mol. Biol. Educ.* **34**, 413–416 (2006).
44. Vigerust, D. J., Vick, S. & Shepherd, V. L. Stable expression and characterization of an optimized mannose receptor. *J. Clin. Cell. Immunol.* **6**, 330 (2015).
45. Llorca, O. Extended and bent conformations of the mannose receptor family. *Cell. Mol. Life Sci.* **65**, 1302–1310 (2008).
46. Gazi, U. & Martinez-Pomares, L. Influence of the mannose receptor in host immune responses. *Immunobiology* **214**, 554–561 (2009).
47. Prigozy, T. I. et al. The mannose receptor delivers lipoglycan antigens to endosomes for presentation to T cells by CD1b molecules. *Immunity* **6**, 187–197 (1997).
48. Mahnke, K. et al. The dendritic cell receptor for endocytosis, Dec-205, can recycle and enhance antigen presentation via major histocompatibility complex class II–positive lysosomal compartments. *J. Cell Biol.* **151**, 673–684 (2000).
49. Jahagirdar, P., Lokhande, A. S., Dandekar, P. & Devarajan, P. V. in *Mannose Receptor and Targeting Strategies* (eds. Jahagirdar, P. et al.) 433–456 (Springer International Publishing, 2019).
50. Tokunaga, M., Imamoto, N. & Sakata-Sogawa, K. Highly inclined thin illumination enables clear single-molecule imaging in cells. *Nat. Methods* **5**, 159–161 (2008).

Methods

Materials. DMEM/F12 medium (HEPES, no phenol red), fetal bovine serum (FBS) and penicillin/streptomycin were purchased from Thermo Fisher Scientific. Geneticin sulfate was purchased from Capricorn Scientific. Culture plates (μ-Slide 8-well glass-bottom) were purchased from Ibidi. SPR sensor chips (no. NiHC1000M) were purchased from XanTec Bioanalytics. The recombinant mouse MR with a C-terminal His-tag for SPR measurements was purchased from Bio-Techne. The NTA regeneration kit was purchased from Cytiva.

Mannoside probe synthesis. The design and synthesis of the probes are discussed in Supplementary information[51–53].

Optical setup. Glyco-PAINT images were obtained using an Oxford Nanoimager microscope (ONI) prewarmed to 37 °C. The sample was illuminated using a TIRF alignment system and fluorescence was recorded using a ×100/1.4-numerical aperture oil immersion objective, passed through a beam splitter. Images were acquired on a 427 × 520-pixel region (pixel size, 0.117 μm) of a sCMOS camera at 50 ms integration time. ATTO655-labeled probes were imaged with a 640-nm laser (40 mW) and ATTO565-labeled probes with a 532-nm laser (40 mW). Thermal drift of the system was determined by tracking 80-nm gold nanoparticles under the same conditions as the actual measurements.

Cell culture. CHO-K1 (ATCC CCL-61) and CHO-MR cells were cultured in a μ-Slide 8-well glass-bottom plate with 400 μl of DMEM/F-12 medium supplemented with 10% FBS, 100 U ml^{-1} penicillin and 100 μg ml^{-1} streptomycin. CHO-MR cells were supplemented with 600 μg ml^{-1} geneticin sulfate. Cells were grown in a standard CO_2 incubator to a confluence of 70–90%.

Super-resolution imaging of the MR with Glyco-PAINT. In preparation for imaging, cells grown on Ibidi 8-well slides were first washed with prewarmed medium. Then, an imaging solution consisting of prewarmed DMEM/F-12 (supplemented with FBS and antibiotics) and labeled mannoside probes was added to the cells. Probe concentration was 5 nM and 20,000 frames were acquired (Fig. 3), while for Figs. 4 and 5 the concentration was adjusted to 1 nM and 10,000 frames were obtained. Negative controls were performed with probe **4** on a MR nonexpressing CHO cell line under the same experimental conditions.

Image and data analysis. Super-resolution images were reconstructed using Oxford Nanoimager software Nimos 1.16. Briefly, a two-dimensional Gaussian was fitted to individual fluorescence spots with at least 300 photons per frame to identify single molecules. Single-particle tracking to obtain MR trajectories was performed with the same software and the following parameters: maximum frame gap, 3; maximum distance between frames, 0.6 μm; exclusion radius, 1.2 μm; and a minimum of two steps per trajectory.

The density of binding events was assessed by counting the number of trajectories within regions of interest formed by following the contour of cells in brightfield images. Then, density was displayed in a color-coded bivariate histogram plot. Data from ten cells randomly selected were collected for quantitative analysis. Statistical significance was assessed by a one-way analysis of variance test.

Residence time was calculated by the duration of each trajectory. Data from 20 cells randomly selected across the sample were combined for each probe to obtain at least 50,000 trajectories, plotted in a histogram and fitted with a single exponential decay function (equation (2)) in OriginLab 2020. From the fitted curve the mean residence time (τ) was obtained. Finally, k_{off} was defined as the inverse of τ (equation (3)):

$$y = y_0 + A_1\, e^{-x/\tau} \tag{2}$$

$$k_{off} = \frac{1}{\tau} \tag{3}$$

The diffusion coefficient of receptors was calculated from the trajectories obtained. To obtain the diffusion coefficient (D), the mean square displacement (MSD) of each trajectory was calculated as in equation (4). Then, equation (5) describes the relation between the diffusion coefficient and MSD, with n the number of dimensions of the data (2) and t the exposure time of the measurement (5×10^{-2} s). As a negative control we used localization precision as x,y displacement to calculate the slowest diffusion that we could calculate with our system:

$$\mathrm{MSD} = \frac{1}{N}\sum_{i=1}^{N}(x_t^i - x_0^i)^2 + (y_t^i - y_0^i)^2 \tag{4}$$

$$\mathrm{MSD} = 2nDt \tag{5}$$

Internalization of probes by imaging. Internalization was measured by imaging cells with an Oxford Nanoimager microscope (ONI) incorporating a HILO[50] illumination arrangement. Cells were grown on an Ibidi 8-well slide and incubated with 20 nM of the probes in growth medium for 2 h at 37 °C. These were then washed with fresh medium and imaged live. Cells were illuminated with a 640-nm laser (16 mW) and a 532-nm laser (10 mW). The brightness and contrast of the resulting TIFF images were adjusted in Fiji software.

Internalization of probes by flow cytometry. Internalization was assessed by flow cytometry in a BD fluorescent activated cell sorter (FACS) Canto II Cell Analyzer. Cells were grown in a 12-well plate to 70–90% confluency and incubated with 1 μM of labeled probes in growth medium for 2 h at 37 °C. Next, they were washed with PBS and trypsinized for 10 min to detach them from the surface. Cells were then centrifuged and resuspended in PBS/bovine serum albumin (1%) to a concentration of 150,000 ml^{-1}. Samples were loaded into the FACS and up to 10,000 cells were analyzed per condition.

Kinetic characterization by SPR. The SPR measurements were performed at 25 °C using a Biacore X100 with a NiHC1000M sensor chip. The NTA regeneration kit consists of 0.5 mM $NiCl_2$ and 350 mM EDTA. SPR running buffers were prepared freshly in ultrapure water and filtered through a 0.2-μm filter.

The recombinant murine MR protein with a C-terminal His-tag was captured on flow cell 2 of a NiHC1000M sensor chip using a running buffer of 25 mM Tris-HCl pH 7.4, 150 mM NaCl and 0.005% P20 surfactant at a flow rate of 10 μl min^{-1}. The chip surface was first conditioned for 1 min with an injection of 0.35 M EDTA before the immobilization procedure. After a 2-min injection of 0.5 mM $NiCl_2$ on flow cell 2, mismatch repair protein (25 μg ml^{-1}) was injected for 2 min to a capture level of around 4,000 RU. Flow cell 1 was left blank as a reference surface. After immobilization, the Biacore X100 was primed with a running buffer of 25 mM Tris-HCl pH 7.4, 150 mM NaCl, 5 mM $CaCl_2$ and 0.005% P20 surfactant. Multicycle kinetics measurements were then conducted at a flow rate of 30 μl min^{-1} for determination of dissociation constants. Two- or fourfold serial dilutions of analyte in the running buffer were injected over the sensor chip for 3 min, followed by dissociation for 5–10 min. Between cycles of single multicycle measurement, no regeneration step was performed due to rapid dissociation of the analyte. After a whole multicycle measurement, the immobilized MR protein was removed with a 2-min injection of 350 mM ETDA and a 2-min injection of 100 mM NaOH, then recaptured on the chip surface for the next measurement of another analyte. Data were corrected by double subtraction to the reference surface (flow cell 1) and buffer injection, and analyzed using a 1:1 interaction fitting model with BIA evaluation software (2020).

Statistics and reproducibility. All experiments shown in Figs. 2–5 and Supplementary Figs 1–5 were repeated three times, with similar results. The experiments shown in Supplementary Fig. 2 were performed once only.

Reporting Summary. Further information on research design is available in the Nature Research Reporting Summary linked to this article.

Data availability

The datasets generated and/or analyzed during the current study are available from the corresponding author on reasonable request.

References

51. Daly, R., Vaz, G., Davies, A. M., Senge, M. O. & Scanlan, E. M. Synthesis and biological evaluation of a library of glycoporphyrin compounds. *Chem. Eur. J.* **18**, 14671–14679 (2012).
52. Wong, C. S., Hoogendoorn, S., van der Marel, G. A., Overkleeft, H. S. & Codée, J. D. C. Targeted delivery of fluorescent high-mannose-type oligosaccharide cathepsin inhibitor conjugates. *ChemPlusChem* **80**, 928–937 (2015).
53. Chan, W. and White, P. *Fmoc Solid Phase Peptide Synthesis: A Practical Approach* (Oxford Scholarship Online, 1999); https://oxford.universitypressscholarship.com/view/10.1093/oso/9780199637256.001.0001/isbn-9780199637256

Acknowledgements

R.R. and L.A. thank the European Research Council/Horizon 2020 for financial support (no. ERC-StG-757397). L.A. thanks NWO for support (VIDI grant no. 192.028). L.A. thanks the Barcelona Institute of Science and Technology for support. This work was funded by the NWO gravitation program 2013 granted to the Institute for Chemical Immunology (no. ICI-024.002.009) (T.P.H. and J.D.C.C.); NWO BBoL grant (W.D.); and the European Research Council (grant no. ERC-CoG-865175, S.I.v.K.).

Author contributions

R.R., T.P.H., J.D.C.C., S.I.v.K. and L.A. conceived the experiments. R.R. performed microscopy. T.P.H. synthesized the probe library. W.D. synthesized propargyl GalNAc **33** and repeated synthesis of certain probes. Y.N. performed SPR experiments. E.B. provided the CHO-MR cell line. The manuscript was written by R.R. and T.H. in consultation with S.P., J.D.C.C., S.I.v.K. and L.A.

Competing interests
The authors declare no competing interests.

Additional information
Supplementary information The online version contains supplementary material available at https://doi.org/10.1038/s41589-021-00896-2.

Correspondence and requests for materials should be addressed to Sander I. van Kasteren or Lorenzo Albertazzi.

Peer review information *Nature Chemical Biology* thanks Khalid Salaita, Ben Schumann and the other, anonymous, reviewer(s) for their contribution to the peer review of this work.

nature research

Corresponding author(s): *Double-blind peer review submissions: write DBPR and your manuscript number here instead of author names.*

Last updated by author(s): *YYYY-MM-DD*

Reporting Summary

Nature Research wishes to improve the reproducibility of the work that we publish. This form provides structure for consistency and transparency in reporting. For further information on Nature Research policies, see our Editorial Policies and the Editorial Policy Checklist.

Statistics

For all statistical analyses, confirm that the following items are present in the figure legend, table legend, main text, or Methods section.

n/a	Confirmed	
☐	☒	The exact sample size (*n*) for each experimental group/condition, given as a discrete number and unit of measurement
☐	☒	A statement on whether measurements were taken from distinct samples or whether the same sample was measured repeatedly
☐	☒	The statistical test(s) used AND whether they are one- or two-sided *Only common tests should be described solely by name; describe more complex techniques in the Methods section.*
☒	☐	A description of all covariates tested
☒	☐	A description of any assumptions or corrections, such as tests of normality and adjustment for multiple comparisons
☐	☒	A full description of the statistical parameters including central tendency (e.g. means) or other basic estimates (e.g. regression coefficient) AND variation (e.g. standard deviation) or associated estimates of uncertainty (e.g. confidence intervals)
☒	☐	For null hypothesis testing, the test statistic (e.g. *F*, *t*, *r*) with confidence intervals, effect sizes, degrees of freedom and *P* value noted *Give P values as exact values whenever suitable.*
☒	☐	For Bayesian analysis, information on the choice of priors and Markov chain Monte Carlo settings
☒	☐	For hierarchical and complex designs, identification of the appropriate level for tests and full reporting of outcomes
☒	☐	Estimates of effect sizes (e.g. Cohen's *d*, Pearson's *r*), indicating how they were calculated

Our web collection on statistics for biologists contains articles on many of the points above.

Software and code

Policy information about availability of computer code

Data collection	Nimos 1.16 is the commercial software used on the Nanoimager microscopy to acquire images.
Data analysis	OriginLab 2020 is used in this study to fit an exponential decay function to dwell times. Fiji (ImageJ) is used to adjust brigthness and contrast of images.

For manuscripts utilizing custom algorithms or software that are central to the research but not yet described in published literature, software must be made available to editors and reviewers. We strongly encourage code deposition in a community repository (e.g. GitHub). See the Nature Research guidelines for submitting code & software for further information.

Data

Policy information about availability of data

All manuscripts must include a data availability statement. This statement should provide the following information, where applicable:

- Accession codes, unique identifiers, or web links for publicly available datasets
- A list of figures that have associated raw data
- A description of any restrictions on data availability

The datasets generated during and/or analysed during the current study are available from the corresponding author on reasonable request.

Field-specific reporting

Please select the one below that is the best fit for your research. If you are not sure, read the appropriate sections before making your selection.

☒ Life sciences ☐ Behavioural & social sciences ☐ Ecological, evolutionary & environmental sciences

For a reference copy of the document with all sections, see nature.com/documents/nr-reporting-summary-flat.pdf

Life sciences study design

All studies must disclose on these points even when the disclosure is negative.

Sample size	No sample-size calculation was performed. We have chosen to obtain at least 100.000 dwell times per sample, which yield a R-squared > 0.98.
Data exclusions	No data was excluded.
Replication	We prepared the samples on 3 different days and obtained the same results.
Randomization	Samples were prepared from the same batch of cells on different wells, and we assigned each sample randomly to each well of cells.
Blinding	There was not blinding on this study. It was not relevant in this study, as conditions for image acquisition and analysis were kept constant through all samples.

Reporting for specific materials, systems and methods

We require information from authors about some types of materials, experimental systems and methods used in many studies. Here, indicate whether each material, system or method listed is relevant to your study. If you are not sure if a list item applies to your research, read the appropriate section before selecting a response.

Materials & experimental systems

n/a	Involved in the study
☒	☐ Antibodies
☐	☒ Eukaryotic cell lines
☒	☐ Palaeontology and archaeology
☒	☐ Animals and other organisms
☒	☐ Human research participants
☒	☐ Clinical data
☒	☐ Dual use research of concern

Methods

n/a	Involved in the study
☒	☐ ChIP-seq
☒	☐ Flow cytometry
☒	☐ MRI-based neuroimaging

Eukaryotic cell lines

Policy information about cell lines

Cell line source(s)	CHO cell expressing MR were obtained through the co-author Evangelia Bolli
Authentication	None of the cell lines were authenticated.
Mycoplasma contamination	All cell lines tested negative for mycoplasma contamination.
Commonly misidentified lines (See ICLAC register)	None misidentified cell line was used in this study.